Broadband and fast photodetectors based on multilayer p-MoTe₂/n-WS₂ heterojunction with graphene electrodes

Wenkai Zhu[1, 2], Faguang Yan[1, 2], Xia Wei[1, 2], Quanshan Lv[1, 2], Huai Yang[1, 2], Kaiyou Wang[1, 2*]

[1]*State Key Laboratory of Superlattices and Microstructures, Institute of Semiconductors, Chinese Academy of Sciences, Beijing, 100083, China*
[2]*College of Materials Science and Opto-Electronic Technology, University of Chinese Academy of Sciences, Beijing, 100049, China*

*Corresponding author: E-mail: kywang@semi.ac.cn

Abstract

Two-dimensional (2D) atomic crystals, such as graphene, black phosphorus and transition metal dichalcogenides (TMDCs) are attractive for use in optoelectronic devices, due to their unique optical absorption properties and van der Waals (vdWs) force between layers. Heterostructures based on layered semiconductors provide a new platform for broadband high performance photodetectors. In this work, graphene-MoTe₂-WS₂-graphene vdWs heterojunctions are fabricated for photodetection. The fundamental electric properties and the band structures of the heterojunctions are investigated and discussed. The devices show a high responsivity ($\approx$ 140 mA W^{-1} at 825 nm), stable and broadband photodetection from UV to NIR wavelength range (300 - 1350 nm), fast response time of 186 µs and self-driven photodetectors. The scanning photocurrent microscopy maps are also employed to study the mechanism of photocurrent generation in the heterojunction. Our results reveal that the vdWs heterojunctions with graphene electrodes offer a new route to broadband detection, optical communication and energy harvesting applications. Copyright © 2019 VBRI Press.

Keywords: Ultraviolet, near-infrared, photodetection, van der Waals heterostructure, molybdenum ditelluride, tungsten disulfide.

Introduction

Broadband photodetector operating in the ultraviolet (UV) to near-infrared (NIR) region have great potential for optoelectronic and energy harvesting applications, such as optical communication, imaging, night vision, environmental monitoring, remote sensing [1-5]. Transition metal dichalcogenides (TMDCs) and other two-dimensional (2D) atomic crystals are attractive for use in optoelectronic devices due to their unique properties, such as favorable electric bandgap, strong light-matter interaction, flexibility, van der Waals assembly, and so forth [6-8]. The ability of stacking them into van der Waals (vdWs) heterostructures has opened a new platform for fundamental research and device applications [9, 10]. Molybdenum ditelluride (MoTe₂) as a member of TMDCs have been extensively discussed. Layered MoTe₂ possesses two stable phases: trigonal prismatic phase (2H) and distorted octahedral phase (1T') [11-14]. Naturally, MoTe₂ shows trigonal (2H) structure, where Mo atoms are sandwiched between two layers of Te atoms, and each Mo is coordinated to six Te atoms [13, 15]. Bulk MoTe₂ (2H-MoTe₂) is a semiconductor with an indirect band gap of about 1.0 eV [16, 17]. MoTe₂ becomes a direct gap semiconductor

with an optical gap of 1.1 eV when the thickness down to monolayer limit [18]. In recent years, the reported few-layered 2H-MoTe₂ field-effect transistors (FETs) shows p-type conducting character under electrical gating and high performance in photodetector applications, such as very high responsivity up to 6A W^{-1} and fast photoresponse of 160 µs [19-23]. In order to reduce the response time, graphene sandwiched MoTe₂ was also fabricated, the device shows a superior performance of high photoresponsivity of 110 mA W^{-1} and very fast response time 24 µs [24]. High-performance photovoltaic photodetectors and interlayer transition based on MoTe₂/MoS₂ vertical heterojunctions were also demonstrated [25, 26]. Tungsten disulfide (WS₂) is another typical TMDCs with n-type conducting and relatively high carrier mobility [27-29]. Similar to MoTe₂, WS₂ is a semiconductor with an indirect bandgap of 1.4 eV and direct bandgap of 2.1 eV in the bulk and monolayer form, respectively [30, 31]. Recently reported results show that WS₂ has great potential for high performance photodetecting applications due to its strong light-matter interaction [27]. In addition, the vdW heterostructure photodetectors with high performance based on WS₂ also have been reported recently [32-34]. In order to achieve high performance

photodetectors with broadband detection, high photoresponsivity and fast response time, p-type $MoTe_2$ and n-type WS_2 were chosen to build the type-II band alignment heterojunction photodetector devices. In this work, we fabricated the multilayer $MoTe_2$-WS_2 vdWs heterojunctions with graphene electrodes using dry-transfer of 2D flakes and site-controllable transfer methods. The devices show high responsivities over a broad spectral range from 300 to 1350 nm, response time down to 186 µs and self-driven photodetectors. Our results show that the vdWs heterojunctions with graphene electrodes could offer a new route to develop broadband and fast photodetectors and next generation photoelectronics.

Experimental

To fabricate the graphene contact $MoTe_2$-WS_2 vdWs heterostructure devices, multiple steps of dry-transfer of 2D flakes method was used. In order to make the p-$MoTe_2$/n-WS_2 vdWs heterojunction, the $MoTe_2$ (from HQ graphene) flake was mechanically exfoliated using adhesive tape from bulk single crystals and subsequently transferred onto a polydimethylsiloxane (PDMS) stamp which is adhered to a glass slide. Under optical microscope, the $MoTe_2$ flake with appropriate thickness and shape can be chose by colors. Afterwards, the target $MoTe_2$ flake was transferred on the SiO_2 (300 nm)/Si^{++} substrate with pre-patterned electrodes by using a site-controllable transfer method. Using the same method, the WS_2 flake was transferred on the top of the $MoTe_2$ flake to fabricate a 2D heterojunction. To reduce the contact resistance, few-layer graphene (FLG) were used as the electrodes [**35**]. The whole transfer processes were performed in a glove box to make a clean interface. The thickness of both $MoTe_2$ and WS_2 flakes were measured by atomic force microscopy (AFM) (Bruker Multimode 8). The device was stored in a small vacuum chamber with 2×10^{-5} mbar during the whole electric and photoelectric measurement processes.

Electrical and optoelectrical properties were measured using a semiconductor characterization system (Agilent Technology B1500A) and a lock-in amplifier (SR830) with a light chopper. The UV light illumination was applied by Xe lamp and the visible to NIR light illumination was provided by a Fianium WhiteLase supercontinuum laser source. The output light was tuned into monochromatic light by an Omni-λ 300 monochromator. A convex lens and an infrared microscope objective lens (Olympus LMPLN IR10×) were used for the UV photoresponse characterization and visible to NIR characterization, respectively. For the spatially-dependent photocurrent measurement, a microscope objective lens (Olympus SLMPLN100×), a lock-in amplifier (SR830) with a light chopper and a micromechanical stage with a control system were used. A home-built measurement system that combined a LED (λ = 470 nm) driven by a square-wave signal generator, a current amplifier (Stanford research systems Model SR570) and a digital oscilloscope (Tektronix TDS

2022B) was used to monitor the response times of the devices.

Results and discussion

Schematic diagram of the p-$MoTe_2$/n-WS_2 heterojunction with graphene electrodes device is presented in **Fig. 1(a)**. The typical AFM image of the partial heterojunction is shown in **Fig. 1(b)**. The inset shows the flattening date that along a line-cut across the heterojunction, indicates the thickness of $MoTe_2$ and WS_2 flakes are 11 nm and 10 nm, respectively. **Fig. 1(c)** show the current-voltage characteristic of the p-$MoTe_2$/n-WS_2 heterojunction device. The device shows a weak rectification behavior. The rectification ratio, defined as the ratio of the forward/reverse current, is about 6 at V_{DS} = +1/-1 V. The inset of **Fig. 1(c)** shows the transfer curves of the Au-$MoTe_2$-Au device for drain bias value V_{DS} = 1 V, which indicate the $MoTe_2$ is p-type conducting materials without gate voltage applied. The thickness of the $MoTe_2$ is about 10 nm in the Au-$MoTe_2$-Au device. The current-voltage characteristic properties of the p-$MoTe_2$/n-WS_2 heterojunction device at different back-gates (V_G) are shown in **Fig. 1(d)**.
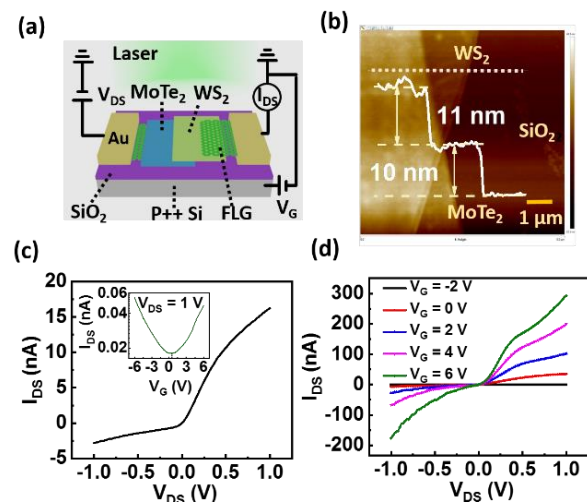
Fig. 1. Schematic diagram and basic properties of p-$MoTe_2$/n-WS_2 heterojunction. (a) Schematic diagram of the p-$MoTe_2$/n-WS_2 heterojunction with graphene electrodes. (b) AFM image of p-$MoTe_2$/n-WS_2 heterojunction device, scale bar 1 µm. The inset shows a line-cut across the heterojunction, indicating the thicknesses of $MoTe_2$ (11 nm) and WS_2 (10 nm). (c) Current-voltage (I-V) characteristics of the device. The inset shows the transfer characteristic of the Au-$MoTe_2$-Au device. (d) Current-voltage characteristic of the device at different gate voltages.

To investigate the responsivity of the device dependence on the illumination intensities, different illumination intensities P ranging from 0 to 5 W cm⁻² are applied to the heterostructure device. The laser beam is focused on the whole device by infrared microscope objective lens (Olympus LMPLN IR 10×) and the diameter of the spot size is about 160 µm, which is larger than the device size. **Fig. 2(a)** shows the output characteristics (I_{DS}-V_{DS}) of the p-$MoTe_2$/n-WS_2 heterojunction under illumination with 825 nm laser at various excitation intensities (P = 0, 0.1, 0.25, 0.5, 1, 2.5,

5 W cm^{-2}). In **Fig. 2(b)**, the I_{DS}-V_{DS} curves of the device with and without laser illumination (825 nm, 5 W cm^{-2}) show clear photovoltaic effect with an open-circuit voltage of ~ 0.1 V and a short-circuit current ~ 16.5 nA.
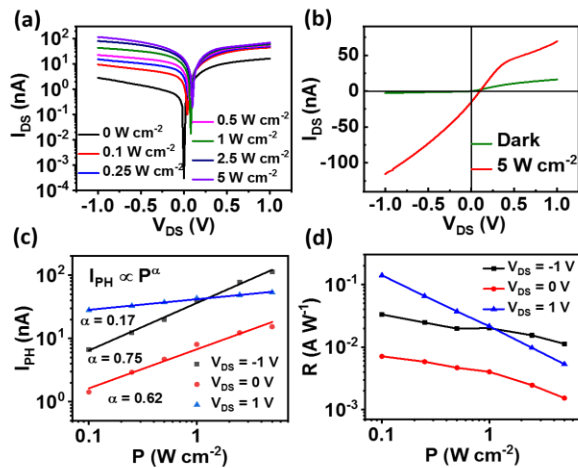
Fig. 2. Power-dependent optoelectronic characterization at different applied voltages V_{DS}. (a) Typical output characteristics (I_{DS}-V_{DS} curves) of the p-MoTe$_2$/n-WS$_2$ heterojunction under illumination with 825 nm laser at various excitation intensities (P = 0, 0.1, 0.25, 0.5, 1, 2.5, 5 W cm^{-2}). The laser beam is focused by infrared microscope objective lens (Olympus LMPLN IR 10×), and the diameter of the spot size is about 160 μm, which is larger than the device size. (b) The I_{DS}-V_{DS} curves of the device with and without laser illumination (825 nm, 5 W cm^{-2}). (c) Photocurrent as a function of the illumination intensity at different V_{DS} (V_{DS} = -1, 0, and 1 V). (d) Responsivities as a function of the illumination intensity at different V_{DS} (V_{DS} = 1, 0, and -1 V).

The photocurrent as a function of the illumination intensity at different V_{DS}. The explanation can be divided into three cases. Under short-circuit state (V_{DS} = 0V), the band diagrams of the p-MoTe$_2$/n-WS$_2$ heterojunction is shown in **Fig. 3(b)**. The built-in field direction is from n-type WS$_2$ to p-type MoTe$_2$. Under illumination of 825 nm laser, the photo-generated electrons and holes in MoTe$_2$ are separated by the built-in field and move into the graphene electrodes in opposite direction across the junction, forming a reversed photocurrent. Under reverse bias (V_{DS} < 0 V), the photocurrent I_{PH} ($I_{PH} = I_{Light} - I_{Dark}$) increases with increasing the light intensity P, and can be enhanced by increasing the reverse bias. It can be explained by the increased electrical field in the heterojunction (**Fig. 3(c)**), which decreases the carrier transit time, thus reducing the recombination of the photo-generated electrons and holes. Under forward bias (V_{DS} > 0 V), the high injection of majority carriers across the heterojunction and the decrease of the barrier in the interface of heterojunction lead to a bigger photocurrent (**Fig. 3(d)**). In **Fig. 2(c)**, the photocurrent I_{PH} shows a sublinear dependence on the incident light intensity P which follows a power law of $I_{PH} \propto P^{\alpha}$, where α = 0.75, 0.62, and 0.17 at source-drain voltages V_{DS} = -1, 0, and 1 V, respectively. The shorter carrier transit time leads to bigger α under reverse bias, while longer carrier transit time leads to a smaller α under forward bias. The similar sublinear behavior has also been reported for other nanomaterials, such as ZnO and GaN nanowires,

WSe$_2$/graphene, MoS$_2$/WS$_2$, WS$_2$/GaSe, InSe/GaSe, WS$_2$/GaSe heterostrctures [29, 36-41]. **Fig. 2(d)** shows the photoresponsivity (R = I_{PH}/PS, where P is the incident light intensity on the device, S is the in-plane area (200 μm^2) of the device) as a function of the illumination intensity at different V_{DS} (V_{DS} = 1, 0, and -1 V). The photoresponsivity decreases with increasing the illumination intensity, which is consistent with the sublinear behavior of the photocurrent. A maximum responsivity R ≈ 140 mA W^{-1} is obtained at V_{DS} = 1 V with an illumination intensity P = 0.1 W cm^{-2} and wavelength λ = 825 nm. The corresponding external quantum efficiency (EQE) is up to 21 %, where EQE (EQE = hcR/eλ) is defined as the ratio of the number of carriers collected by the electrodes to the number of incident photons, h and c are Plank constant and speed of light. The photoresponsivity is comparable to most of similar vdWs heterojunction photodetectors reported very recently, such as 110 mA W^{-1} in Graphene/MoTe$_2$/Graphene and 4.36 mA W^{-1} in MoS$_2$/WS$_2$ [24, 33].
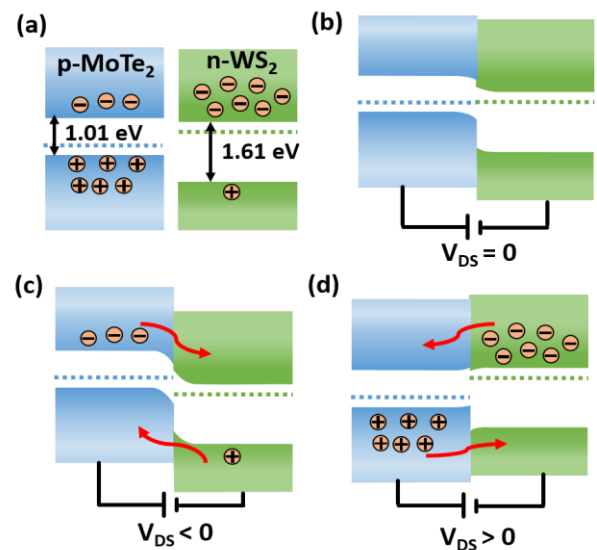
**Fig. 3.** Schematic band diagrams at the interface of the p-MoTe$_2$/n-WS$_2$ heterojunction. (a) Band diagram of the isolated p-MoTe$_2$ and n-WS$_2$, electron affinities of p-MoTe$_2$ and n-WS$_2$ are about -3.77 eV and -3.92 eV, respectively. (b-d) Schematic band alignment at the interface of the heterojunction at different applied voltages V_{DS} (zero bias (b), reverse bias(c), and forward bias (d)).

Fig. 3(a) shows the band diagram of the isolated p-MoTe$_2$ and n-WS$_2$. The electron affinities of p-MoTe$_2$ and n-WS$_2$ are about -3.77 and -3.92 eV, respectively [42, 43]. The conduction minimum (CB) of p-MoTe$_2$ lies above that of n-WS$_2$ by ΔE_c = 0.15 eV whereas the valence band (VB) edge of n-WS$_2$ lies below (ΔE_v = 0.75 eV) that of p-MoTe$_2$, resulting in a type-II band alignment. The built-in potential is formed when stack them into heterostructure as shown in **Fig. 3(b)**. **Fig. 3(c)** shows the electrical field in the heterojunction is strongly enhanced under reverse bias. **Fig. 3(d)** shows the barrier in the interface of p-MoTe$_2$/n-WS$_2$ heterojunction is decreased under forward bias.
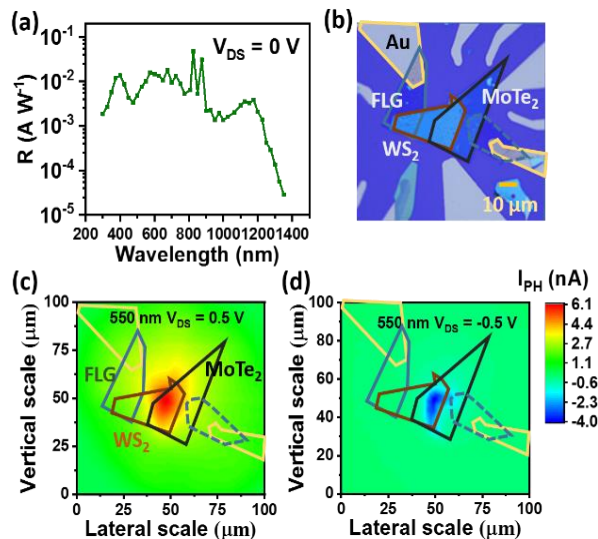
Fig. 4. Photoresponse of the p-MoTe$_2$/n-WS$_2$ heterojunction. (a) Room temperature photoresponsivity (R) as a function of illumination wavelength (λ) at zero bias and illumination intensity P = 0.01 W cm^{-2}. (b) Optical microscope image of the heterojunction, component materials are outlined in different colors. (c-d) Scanning photocurrent microscope images of the p-MoTe$_2$/n-WS$_2$ heterojunction at V$_{DS}$ = 0.5 V (c) and -0.5 V (d) with illumination wavelength 550 nm (PS = 1 μW) respectively. The blue dotted and solid lines outline the bottom and top of graphene electrodes, the black solid line outlines the MoTe$_2$ sheet and dark orange solid line outlines the WS$_2$ sheet, respectively. The laser beam is focused by microscope objective lens (Olympus SLMPLN100×) and the diameter of the spot size is about 2 μm.

The spectral dependent photoresponsivity of the p-MoTe$_2$/n-WS$_2$ heterojunction shown in **Fig. 4(a)** which illustrate a high photoresponsivity over the range of λ = 300 - 1350 nm, from UV to NIR, under zero bias with illumination intensity P = 0.01 W cm^{-2}. At zero bias, the device has a maximum photoresponsivity (R) of R = 48 mA W^{-1}, and the corresponding external quantum efficiency (EQE) is up to 7.2% at λ = 825 nm. The device can work in special environment as a self-driven photodetector with broadband photodetection. In order to explore the origin of the photoresponse, scanning photocurrent microscope image method is employed at both forward and reverse biases. The scanning area is shown in **Fig. 4(b)** with the optical microscope image of the heterojunction. The different materials are outlined by different lines and colors. The blue dotted and solid lines outline the bottom and top of graphene electrodes, the black solid line outlines the MoTe$_2$ sheet and dark orange solid line outlines the WS$_2$ sheet, respectively. The laser beam is focused by microscope objective lens (Olympus SLMPLN100×) and the diameter of the spot size is about 2 μm. The corresponding photocurrent mapping at forward and reverse biases with illumination wavelength of 550 nm (PS = 1 μW) are presented in **Fig. 4(c)** and **Fig. 4(d)**, respectively. The most sensitivity of photoresponse is found in the overlapping region of the p-MoTe$_2$ and n-WS$_2$ flakes, which indicates that the p-n junction can play a critical role in photoresponse.
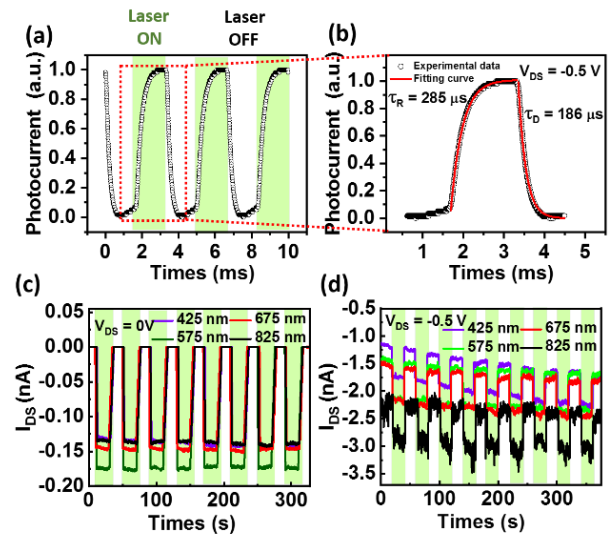
Fig. 5. Temporal photoresponse and photo-switching of the p-MoTe$_2$/n-WS$_2$ heterojunction. (a), (b) Normalized time response and rise time (τ$_R$) and decay time (τ$_D$) at V$_{DS}$ = -0.5 V under light diode illumination. The red solid lines are fits to the experimental date. (c), (d) Source-drain current I$_{DS}$ as a function of time with photoswitching at V$_{DS}$ = 0 V and -0.5 V under illumination with different wavelengths 425, 575, 675, and 825 nm (P = 0.01 W cm^{-2}).

The response time is an important factor to characteristic the performance of a photodetector. For investigate the respond speed and stability of the device, the device was illuminated by a LED (λ = 470 nm) driven by a square-wave signal generator and the dynamic response of the photocurrent was obtained by a current amplifier and a digital oscilloscope. **Fig. 5(a)** shows the normalized time response of the p-MoTe$_2$/n-WS$_2$ heterojunction at the reverse bias V$_{DS}$ = -0.5V. The dynamic response of the photocurrent is described well by the equations I(t) = I$_0$[1- exp(-(t-t$_0$)/τ$_R$)] and I(t) = I$_0$exp[-(t-t$_0$)/τ$_D$], where τ$_R$ and τ$_D$ are the rise time and decay time constants, t$_0$ is the time laser on/off, I$_0$ is the constant. In **Fig. 5(b)**, τ$_R$ and τ$_D$ is calculated to be 285 μs and 186 μs by fitting the rising and falling edges, the red solid lines are fitting results. The response time is comparable to most recently reported similar vdWs heterojunction photodetectors, such as 50 ms in GaSe/MoS$_2$, 670 μs in WS$_2$/Si, 100 μs in WSe$_2$/MoS$_2$.[**44-46**] At zero bias, τ$_R$ and τ$_D$ is calculated to be 3.03 ms and 3.07 ms using the same method. The shorter response time at V$_{DS}$ = -0.5 V is attribute to the stronger electric field at the interface of the p-MoTe$_2$/n-WS$_2$ heterojunction in reverse bias. **Fig. 5(c)** and **(d)** show that the photocurrent can be switched on and off stably and repeatedly with a square-wave modulation light intensity for different laser wavelength (λ = 425, 575, 675, and 825 nm) at an illumination power P = 0.01 W cm^{-2}. In **Fig. 5(c)**, the p-MoTe$_2$/n-WS$_2$ heterojunction device can generate a self-powered photocurrent at zero bias voltage, due to the type-II band alignment and the graphene electrodes. It is worth noting, the device exhibits a stable and fast photoresponse to the incident laser with a considerable ON/OFF ratio up to 10^3.

Conclusion

In conclusion, we have fabricated the $MoTe_2$-WS_2 vdWs heterojunctions with graphene electrodes by using dry-transfer of 2D flakes method. The devices exhibit high responsivity over a broad spectral range of 300 - 1350 nm and can work in special environment as a self-driven photodetector. A maximum responsivity $R \approx 140$ mAW^{-1} is obtained with an illumination intensity $P = 0.1$ W cm^{-2} and wavelength $\lambda = 825$ nm. The corresponding external quantum efficiency (EQE) is up to 21 %. The device also shows a fast response time of 186 µs. The scanning photocurrent microscopy maps show the most sensitivity of photoresponse area is the overlapping region of the p-n heterojunction. Our work suggests that vdWs heterojunction with graphene electrodes has promising applications in next generation broadband photodetectors.

Author's contributions

Conceived the plan: K.Y. Wang, F.G. Yan; Performed the experiments: W.K. Zhu, F.G. Yan; Data analysis: W.K. Zhu, F.G. Yan; Wrote the paper: W.K. Zhu, F.G. Yan, X. Wei, Q.S. Lv, H. Yang. All authors participated in scientific discussion. Authors have no competing financial interests.

References

1. Schermelleh, L., et al.; *Science*, **2008**, *320*, 1332.
   DOI: 10.1126/science.1156947.
2. Radisavljevic, B.; Radenovic, A.; Brivio, J.; Giacometti, V.; Kis, A., *Nature Nanotechnology*, **2011**, *6*, 147.
   DOI: 10.1038/nnano.2010.279
3. Konstantatos, G.; Sargent, E. H., *Nature Nanotechnology*, **2010**, *5*, 391.
   DOI: 10.1038/nnano.2010.78.
4. Huang, Y.; Duan, X., *Small*, **2005**, *1*, 142.
   DOI: 10.1002/smll.200400030.
5. Formisano, V.; Atreya, S.; Encrenaz, T.; Ignatiev, N.; Giuranna, M.; *Science*, **2004**, *306*, 1758.
   DOI: 10.1126/science.1101732.
6. Bernardi, M.; Palummo, M.; Grossman, J. C.; *Nano Letters*, **2013**, *13*, 3664.
   DOI: 10.1021/nl401544y.
7. Britnell, L.; Ribeiro, R.M., *Science*, **2013**, *340*, 1311.
   DOI: 10.1126/science.1235547.
8. Luo, W., et al.; *Advanced Optical Materials*, **2015**, *3*, 1418.
   DOI: 10.1002/adom.201500190.
9. Yan, F., et al.; *Small Methods*, **2018**, *2*, 1700349.
   DOI: 10.1002/smtd.201700349.
10. Wei, X.; Yan, F.; Lv, Q.; Wang, K.; *Chinese Physics B*, **2017**, *26*, 038504.
11. Beal, A. R.; Hughes, H. P.; *Journal of Physics C: Solid State Physics*, **1979**, *12*, 881.
12. Park, J. C., et al.; *ACS Nano*, **2015**, *9*, 6548.
    DOI: 10.1021/acsnano.5b02511.
13. Yin, L., et al.; *Applied Physics Letters*, **2016**, *108*, 043503.
    DOI: 10.1063/1.4941001.
14. Keum, D. H., et al.; *Nature Physics*, **2015**, *11*, 482.
    DOI: 10.1038/nphys3314
15. Lin, Y., et al.; *Advanced Materials*, **2014**, *26*, 3263.
    DOI: 10.1002/adma.201305845.
16. Grant, A. J.; Griffiths, T. M.; Pitt, G. D.; Yoffe, A. D., *Journal of Physics C: Solid State Physics*, **1975**, *8*, L17.
17. Conan, A.; Delaunay, D.; Bonnet, A.; Moustafa, A. G.; Spiesser, M., *Physica Status Solidi (b)*, **1979**, *94*, 279.
    DOI: 10.1002/pssb.2220940132.
18. Ruppert, C.; Aslan, O. B.; Heinz, T. F., *Nano Letters*, **2014**, *14*, 6231.
    DOI: 10.1021/nl502557g.
19. Octon, T. J.; Nagareddy, V. K.; Russo, S.; Craciun, M. F.; Wright, C. D., *Advanced Optical Materials*, **2016**, *4*, 1750.
    DOI: 10.1002/adom.201600290.
20. Pradhan, N. R., et al.; *ACS Nano*, **2014**, *8*, 5911.
    DOI: 10.1021/nn501013c.
21. Fathipour, S., et al.; *Applied Physics Letters*, **2014**, *105*, 192101.
    DOI: 10.1063/1.4901527.
22. Liu, J., et al.; *Nanoscale Research Letters*, **2018**, *13*, 291.
    DOI: 10.1186/s11671-018-2721-0.
23. Duong, N. T., et al.; *Nanoscale*, **2018**, *10*, 12322.
    DOI: 10.1039/C8NR01711E.
24. Zhang, K., et al.; *ACS Applied Materials & Interfaces*, **2017**, *9*, 5392.
    DOI: 10.1021/acsami.6b14483.
25. Zhang, K., et al.; *ACS Nano*, **2016**, *10*, 3852.
    DOI: 10.1021/acsnano.6b00980.
26. Chen, Y., et al.; *Small (Weinheim an der Bergstrasse, Germany)*, **2018**, *14*.
    DOI: 10.1002/smll.201703293.
27. Iqbal, M. W., et al.; *Scientific Reports*, **2015**, *5*, 10699.
    DOI: 10.1038/srep10699
28. Tan, H., et al.; *ACS Nano*, **2016**, *10*, 7866.
    DOI: 10.1021/acsnano.6b03722.
29. Lv, Q.; Yan, F.; Wei, X.; Wang, K., *Advanced Optical Materials*, **2018**, *6*, 1700490.
    DOI: 10.1002/adom.201700490.
30. Zeng, H., et al.; *Scientific Reports*, **2013**, *3*, 1608.
    DOI: 10.1038/srep01608
31. Berkdemir, A., et al.; *Scientific Reports*, **2013**, *3*, 1755.
    DOI: 10.1038/srep01755.
32. Huo, N., et al.; *Advanced Functional Materials*, **2014**, *24*, 7025.
    DOI: 10.1002/adfm.201401504.
33. Wu, W., et al.; *Nano Energy*, **2018**, *51*, 45-53.
34. Lan, C., et al.; *Journal of Materials Chemistry C*, **2017**, *5*, 1494.
    DOI: 10.1039/C6TC05037A.
35. Du, Y., et al.; *IEEE Electron Device Letters*, **2014**, *35*, 599.
    DOI: 10.1109/LED.2014.2313340.
36. Massicotte, M., et al.; *Nature Nanotechnology*, **2015**, *11*, 42.
    DOI: 10.1038/nnano.2015.227
37. Soci, C., et al.; *Nano Letters*, **2007**, *7*, 1003.
    DOI: 10.1021/nl070111x.
38. González-Posada, F.; Songmuang, R.; Den Hertog, M.; Monroy, E.; *Nano Letters*, **2012**, *12*, 172.
    DOI: 10.1021/nl2032684.
39. Xue, Y., et al.; *ACS Nano*, **2016**, *10*, 573.
    DOI: 10.1021/acsnano.5b05596.
40. Yan, F., et al.; *Nanotechnology*, **2017**, *28*, 27LT01.
41. Wei, X.; Yan, F.; Lv, Q.; Shen, C.; Wang, K.; *Nanoscale*, **2017**, *9*, 8388.
    DOI: 10.1039/C7NR03124F.
42. Kang, J.; Tongay, S.; Zhou, J.; Li, J.; Wu, J., *Applied Physics Letters*, **2013**, *102*, 012111.
    DOI: 10.1063/1.4774090.
43. Li, M., et al.; *Nanotechnology*, **2018**, *29*, 335203.
44. Islam, A.; Lee, J.; Feng, P. X. L.; *ACS Photonics*, **2018**, *5*, 2693.
    DOI: 10.1021/acsphotonics.8b00318.
45. Lan, C., et al.; *ACS Applied Materials & Interfaces*, **2016**, *8*, 18375.
    DOI: 10.1021/acsami.6b05109.
46. Cheng, R., et al.; *Nano Letters*, **2014**, *14*, 5590.
    DOI: 10.1021/nl502075n.